Nanosecond Time-Resolved Microscopic Gate-Modulation Imaging of Polycrystalline Organic Thin-Film Transistors

Satoshi Matsuoka,[1,2,*] Jun'ya Tsutsumi,[2,†] Hiroyuki Matsui,[3] Toshihide Kamata,[1,2] and Tatsuo Hasegawa[2,4,‡]

[1]*Graduate School of Pure and Applied Sciences, University of Tsukuba, 1-1-1 Tennoudai, Tsukuba 305-8571, Japan*

[2]*National Institute of Advanced Industrial Science and Technology (AIST), Tsukuba Central 5, 1-1-1 Higashi, Tsukuba 305-8565, Japan*

[3]*Research Center for Organic Electronics (ROEL), Graduate School of Organic Materials Science, Yamagata University, 4-3-16 Jonan, Yonezawa, 992-8510, Japan*

[4]*Department of Applied Physics, The University of Tokyo, 7-3-1 Hongo, Bunkyo-ku, Tokyo 113-8656, Japan*

(Received 1 October 2017; revised manuscript received 11 January 2018; published 23 February 2018)

We develop a time-resolved microscopic gate-modulation (μGM) imaging technique to investigate the temporal evolution of the channel current and accumulated charges in polycrystalline pentacene thin-film transistors (TFTs). A time resolution of as high as 50 ns is achieved by using a fast image-intensifier system that could amplify a series of instantaneous optical microscopic images acquired at various time intervals after the stepped gate bias is switched on. The differential images obtained by subtracting the gate-off image allows us to acquire a series of temporal μGM images that clearly show the gradual propagation of both channel charges and leaked gate fields within the polycrystalline channel layers. The frontal positions for the propagations of both channel charges and leaked gate fields coincide at all the time intervals, demonstrating that the layered gate dielectric capacitors are successively transversely charged up along the direction of current propagation. The initial μGM images also indicate that the electric field effect is originally concentrated around a limited area with a width of a few micrometers bordering the channel-electrode interface, and that the field intensity reaches a maximum after 200 ns and then decays. The time required for charge propagation over the whole channel region with a length of 100 μm is estimated at about 900 ns, which is consistent with the measured field-effect mobility and the temporal-response model for organic TFTs. The effect of grain boundaries can be also visualized by comparison of the μGM images for the transient and the steady states, which confirms that the potential barriers at the grain boundaries cause the transient shift in the accumulated charges or the transient accumulation of additional charges around the grain boundaries.

DOI: 10.1103/PhysRevApplied.9.024025

I. INTRODUCTION

Because of their superior processability and greater productivity, polycrystalline semiconductor thin films are superior to single crystals for applications in large-area electronics devices [1–3]. Actual examples are found in a variety of semiconductor devices based on, for example, polycrystalline silicon [1,4–6], indium gallium zinc oxide [7,8], carbon nanostructures [9,10], organic-inorganic hybrid materials [11–13], or organic semiconductors [3,14–16]. The carrier-transport characteristics of these polycrystalline thin films should be considerably affected by grain boundaries, in addition to the finite size effects of semiconductors within the respective microcrystalline grains [17]. In particular, carrier transport through the lateral conduction paths within polycrystalline thin films has a marked effect on the device characteristics of thin-film transistors (TFTs). These effects naturally hold for organic TFTs, even though their channel layers are composed of molecular assemblies formed by weak van der Waals intermolecular interactions, so that grain boundaries between microcrystals are expected to have weaker effects than those in other materials [18–20]. Nevertheless, the microscopic carrier transport through polycrystalline semiconductors is inadequately understood, mainly because experimental probing of local carrier transport has been difficult for assemblies of tiny microcrystals with sizes of the order of 1 μm.

We recently succeeded in developing a high-resolution microscopic gate-modulation (μGM) imaging technique that permits the visualization of the spatial distribution of charge-carrier densities within the semiconducting channel

*matsuoka-s@aist.go.jp
†junya.tsutsumi@aist.go.jp
‡t-hasegawa@aist.go.jp

layers of polycrystalline organic TFTs [21]. The technique relies on highly sensitive difference-image sensing between alternately biased gate-on and gate-off states through visualization of the resulting small changes in the local optical absorption of the channel layers. The resulting images basically reflect the spatial distribution of accumulated charges within the channel layers [21–25]. Additionally, μGM images acquired at a specific photon energy of 1.85 eV for polycrystalline pentacene TFTs indicate that two distinct effects appear simultaneously as negative and positive μGM signals within the polycrystalline channel layers. Spectroscopic analyses based on a series of μGM images obtained at various photon energies reveals that the negative and positive μGM signals at 1.85 eV can be attributed to the effects of charge accumulation and leaked gate fields, respectively. Comparisons of the μGM images with the observed polycrystalline morphologies indicate that grain centers predominately correspond to areas with high leaked gate fields, due to the low charge density, whereas grain edges correspond predominantly to areas with a high charge density with a certain spatial extension, probably associated with the concentrated carrier-trap distributions. These analyses clearly demonstrate the roles of grain boundaries in the carrier-transport characteristics of polycrystalline pentacene TFTs.

The μGM images described above are obtained at steady states only [21]. By taking advantage of the rapid response of the μGM imaging technique, it should be possible to probe the charge-carrier dynamics within the channel layers more directly, in addition to the steady-state observations. The dynamic carrier transport through the channel layers of organic TFTs has previously been probed by other techniques, such as optical pump-probe techniques [26,27] or the second-harmonic-generation imaging technique [28,29]. However, it is still unclear how carrier transport is affected or modulated by the limiting factors in polycrystalline channel layers, because the existing techniques are incapable of probing charge carriers directly. Therefore, the use of the μGM imaging techniques should be more informative in revealing how charge carriers prevail and propagate in polycrystalline channels.

In this paper, we focus on the transient aspects of carrier transport in the channel layers of polycrystalline pentacene TFTs, by means of the nanosecond time-resolved–microscopic-gate-modulation (TR-μGM) imaging technique. For this purpose, we successfully establish high temporal resolution for the TR-μGM imaging technique of as little as 50 ns through the use of the combination of fast image-sensing technologies. Here, we first describe the experimental technique for the realization of our nanosecond TR-μGM imaging technique. We then present our experimental results obtained by fast μGM imaging, which clearly visualizes the gradual propagation of both the accumulated charges and leaked gate fields within the channel layers of polycrystalline pentacene TFTs. On the basis of these TR-μGM images, we discuss the overall appearance of the signals in the TR-μGM images, the correlation between mobility and channel-front propagation, the peculiar transient features of charge and field distribution at channel-electrode interfaces, and the effects of grain boundaries on transient charge and field distributions.

II. EXPERIMENTAL

Highly pure pentacene (purified three times by vacuum sublimation) is purchased from the NARD Institute Ltd. (Hyogo, Japan). For nanosecond TR-μGM imaging measurements, polycrystalline pentacene TFTs are fabricated on an *n*-doped Si wafer (0.5-mm thick) with a 100-nm-thick layer of SiO_2, in which the Si and SiO_2 layers are used as the gate electrode and the gate dielectric layer, respectively. The device structure has a bottom-gate top-contact configuration with a channel length of 100 μm and channel width of 1 mm. A 50-nm-thick channel pentacene layer is deposited at an evaporation rate of 0.01 $nm\,s^{-1}$ and a substrate temperature of 343 K under a pressure of 10^{-5} Pa, resulting in the growth of dendritic crystalline grains with an average size of 3.2 μm [21]. Gold source and drain electrodes of 30-nm thick are deposited and formed on the pentacene channel layer in vacuum. The devices are finally encapsulated by a 200-nm-thick polymer layer of Parylene C to prevent the degradation of the pentacene layer by oxygen or moisture. The fabricated devices show a field-effect mobility of 1.0 $cm^2\,V^{-1}\,s^{-1}$ in the saturation regime (see Fig. S1 in the Supplemental Material [30]). All the device-fabrication processes are carried out in a glovebox filled with inert N_2 gas.

The TR-μGM imaging measurements are conducted by using a self-assembled apparatus composed of an optical microscope equipped with a complementary metal-oxide-semiconductor (CMOS) image sensor, an image intensifier, and a pulsed light-emitting diode (LED), as shown in Fig. 1(a). In the measurements, the TFT is illuminated by the LED light with a pulse length of 20 μs and a photon energy of 1.88 eV, and the reflected light is captured as an optical microscopy image by the CMOS image sensor after amplification by the image intensifier. Note that the μGM images obtained at 1.88 eV (used in this study) and 1.85 eV (used in a previous study [21]) give basically the same spatial distributions of positive and negative μGM signals, although the μGM signal intensity at 1.88 eV is about 20% less than that at 1.85 eV.

Note that all the TR-μGMI measurements are conducted with electrically grounded source electrode and electrically floated drain electrode, in order to focus on the observation of diffusion current that originates from the concentration gradient of charge-carrier density in the channel. This is because the diffusion current should reflect the intrinsic transport properties more directly, and should be also independent of the drain bias, in contrast to the drift current. In this measurement condition, carrier injections should take place only from the source electrode, and

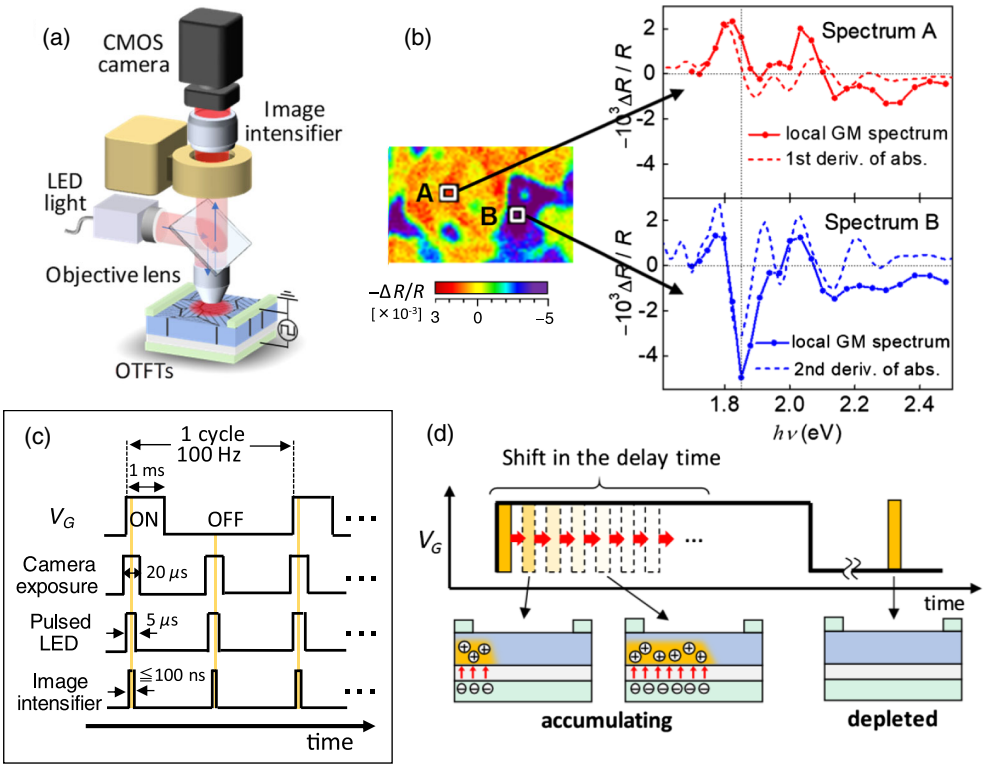

FIG. 1. (a) Schematic representation of the experimental setup for the TR-μGM imaging measurements. (b) GM spectra at local areas showing positive (A) and negative (B) signals in the μGM images at 1.85 eV. (c) Trigger timing of the gate voltage application, camera exposure, LED lightning, and image intensifier operation. (d) Schematic showing the measurement principle for the TR-μGM imaging.

they should propagate unidirectionally from the source electrode, which can simplify the analyses of the results. In contrast, in the case that the drain bias is applied, it is assumed to add the drift current in the channel by the electric field between source and drain electrodes. We consider that the analyses of the measurements should be more complicated than the above. Additionally, in the case that both source and drain electrodes are electrically grounded, carrier injections should take place from both electrodes into the channel layer, and they should propagate diffusively from both sides toward the center of the channel.

A pulsed gate-bias modulation, switched between 0 and −40 V at 100 Hz, is applied to the gate electrode with the pulse length of 1 ms. The reflected light images are captured at a frequency of 200 Hz for both gate-on and gate-off states; the resulting differential image is integrated and averaged over a number of cycles to obtain the final μGM image ($-\Delta R/R$);1.6×10^6 cycles are averaged for the measurements at a time resolution of 100 ns, and 6.4×10^6 cycles are averaged for those at a time resolution of 50 ns. The timings of the camera exposure, the LED emission, and the image-intensifier operation are adjusted to match one another. The total time resolution is determined by the operating time of the image intensifier, which is set at 100 or 50 ns. The TR-μGM images are measured by delaying the operation timing of the image intensifier after turning on the gate bias, whereas those obtained after turning off the gate bias are fixed at 4 ms, as schematically shown in Figs. 1(c) and 1(d). The spatial resolution of the TR-μGM image is less than 500 nm at a photon energy of 1.88 eV; this is basically determined by the numerical aperture (NA) of the objective lens (NA = 0.95).

III. RESULTS AND DISCUSSIONS

A. Time-resolved microscopic gate-modulation images

Figure 2 shows the optical microscopic and the corresponding TR-μGM images of the polycrystalline pentacene TFTs obtained at delay time shifts from 100 to 500 ns at intervals of 100 ns after the gate bias is turned on. The measurements are conducted with a time resolution of 100 ns. A μGM image obtained at a delay time of 500 μs, corresponding to a (nearly) steady-state image, is also presented in the figure. The positive (red-colored) and negative (blue-colored) μGM signals are distributed inhomogeneously in all the images. We also find that the positions of positive and negative μGM signals in the transient-state images coincide well with those in the steady-state image.

In the previous report, the origin of the positive and negative μGM signals in the steady-state image is discussed intensively: Spectroscopic analyses based on a series of steady-state μGM imaging measurements at various photon energies reveal that the positive μGM signals originate from the first-derivative-like GM spectrum [as shown by the positive signal at 1.88 eV in spectrum A of Fig. 1(b)], whereas the negative μGM signals originate from the second-derivative-like GM spectrum (as shown by the negative signal at 1.88 eV in spectrum B of Fig. 1(b)].

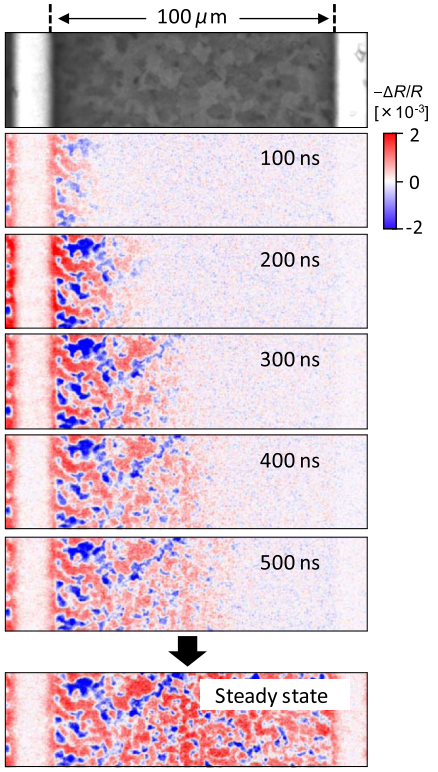

FIG. 2. Optical micrograph and the corresponding TR-μGM images at various delay times captured with a time resolution of 100 ns. The steady-state image is measured at a delay time of 500 μs.

It is also pointed out that the very similar first- and second-derivative-like spectra are also observed in the "macroscopic" GM spectroscopy for polycrystalline pentacene TFTs, depending on the polarity of the applied gate biases [31]. It is discussed that the former is obtained by electric-field modulation in the channels without charge accumulation through applying the positive gate-bias modulation, whereas the latter is obtained by charge-density modulation through applying the negative gate-bias modulation. Then the former causes a slight shift of the absorption spectrum as a result of a quadratic Stark effect, which eventually affords the first-derivative-like spectrum (which corresponds to the electroabsorption spectrum [31,32]). In contrast, the negative gate-bias modulation causes the second-derivative-like spectrum whose origin is more complicated, partly because the spectral shape seems to be intermediate between absorption bleaching and second-derivative-like spectrum. On the origin of the second-derivative-like spectrum, it is discussed that the spectral broadening of the exciton absorption is derived from the charge accumulation in polymeric semiconductors, as associated with the violation of exciton-coupling effects [33]. Nonetheless, the second-derivative-like feature, as observed in the microscopic GM spectrum, is much clearer than the conventional macroscopic GM spectrum, and should be clearly ascribed to the effect of charge accumulation.

Based on these arguments, it is concluded that the origin of the inhomogeneous distribution of the positive and negative μGM signals as observed in the steady-state image could be understood under an assumption that the gate electric field is not shielded in specific local areas of low charge density, but instead leaks into the channel layers [21]. A markedly inhomogeneous charge distribution should be associated with the sparse presence of concentrations of charge traps in the polycrystalline pentacene thin films. We also note here that we clearly observe a linear relationship between the modulated gate bias and the (both positive and negative) μGM signals, at least within a limited range for the clear observation of the steady-state μGM images. This implies that both of the positive and negative μGM signals should be associated with the average charge-carrier concentration, as a whole, in the channel.

In the TR-μGM images, we find that the positions of positive and negative μGM signals coincide well with those in the steady-state image. It implies that the distribution of charge traps in the channel is inherent and fixed, and should be determined by the polycrystalline morphologies. We also clearly observe that the areas of both the positive and negative μGM signals gradually and simultaneously expanded in the channel. The frontal positions of the accumulated charges and leaked gate fields gradually expanded or propagate toward the counterelectrodes as time passes. The lateral-line profiles of the TR-μGM images are shown in Fig. 3(a); the positive and negative μGM signals at each lateral position are averaged over all the vertical pixels in the TR-μGM images to obtain the red and blue profiles, respectively. The μGM intensities at the corresponding positions are divided by the steady-state μGM intensities at identical positions obtained at a delay time of 500 μs. This confirms that the charge front and the field front are identical at a given timing, as shown by extrapolating the linear fit of the μGM signal (green lines) to the zero baseline (the intercept of which is indicated by the arrows) in Fig. 3(a). In contrast, the μGM signals (white colored) are very small at the right side of the charge and the field front in the TR-μGM images obtained at the various time intervals (see Fig. 2). This shows that the leaked gate fields are apparently absent just after switching on the gate bias, but are generated into the channels after the accumulation of local charge carriers. We conclude that local electric fields within the gate dielectric layers become effective only when hole carriers are present in the channels, and consequently excess electrons in the gate electrodes charge up at both sides of the gate dielectric layers, as shown schematically in Fig. 4(a). These transient phenomena will be modeled and analyzed below. We also comment here that this type of channel charge accumulation is a unique characteristic of organic TFTs whose channels are composed of intrinsic semiconductors in which the gate fields are not terminated but penetrate into the channel layers.

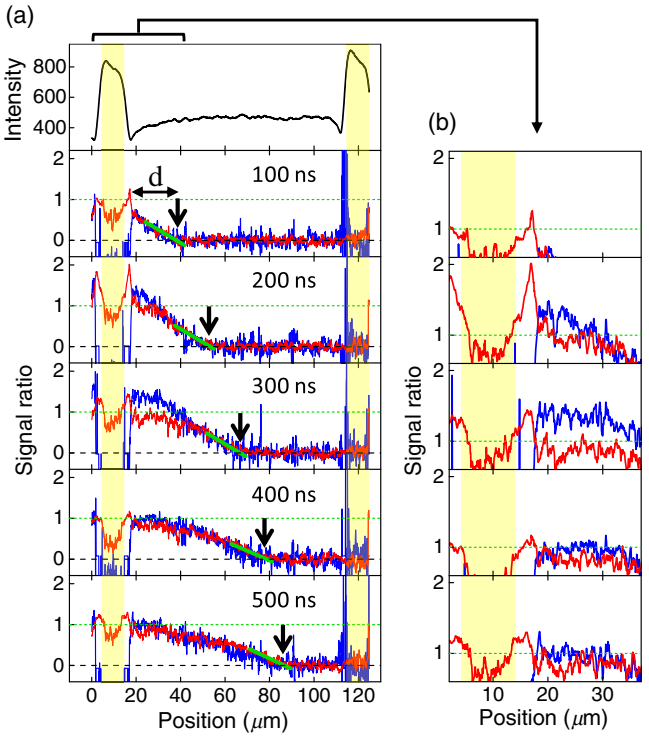

FIG. 3. (a) The lateral line profiles of TR-μGM images (Fig. 2) whose intensity is divided by that in the steady state. The red and blue lines indicate the positive and negative μGM signals. The black arrows indicate the frontal positions of the channel determined by extrapolating the linear fit (green line) to the zero baseline. The yellow regions correspond to the source and drain electrodes. (b) The expanded line profile near the source electrode.

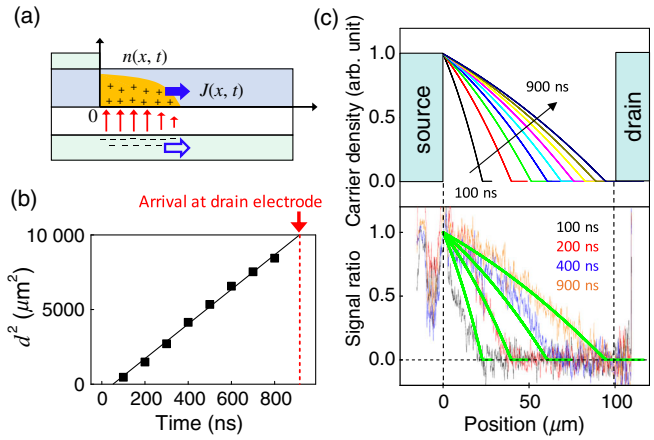

FIG. 4. (a) Schematic representation of the transient carrier distribution in a TFT. (b) The square of the distance from the source electrode to the frontal position of the channel plotted as a function of time. (c) Transient carrier distribution simulated by the temporal-response model of TFTs (upper graph) and a comparison with the experimental results for a positive μGM signal (lower graph).

B. Correlation between mobility and channel-front propagation

We examine the correlation between field-effect device characteristics and the transient behavior of channel-front propagation. The frontal positions of the accumulated charges and leaked gate fields are identical to one another, as discussed above. Figure 4(b) shows the square of the distance d between the frontal positions and the electrode edge, plotted as a function of time. A linear correlation between d^2 and t is clearly observed, implying an apparent diffusional motion of charge carriers in the channels [34]. By extrapolating the linear fit of the data to 10 000 μm^2, the transit time of the front line between the electrodes is estimated at 900 ns for the whole channel length of 100 μm.

As discussed above, the local gate electric fields become effective after the frontal position of the channel charges is reached [see Fig. 4(a)]. This means that the layered gate dielectric capacitors are charged successively along the direction of propagation of the current in a transverse fashion. To analyze the charge-carrier dynamics in the channels of the TFTs precisely, we simulate the transient carrier distribution under the gradual channel approximation. The three physical quantities of carrier density $n(x,t)$, current density $J(x,t)$, and electric potential $V(x,t)$ within the channels are defined as a function of the time t and the position x. First, the carrier density is directly associated with the electric potential by the capacitance of the gate dielectric layer, as follows:

$$n(x,t) = \frac{C\{V(x,t) - (V_{\rm G} - V_{\rm th})\}}{e}, \qquad (1)$$

where C is the capacitance of the gate insulator, V_G and $V_{\rm th}$ are the gate voltage and the threshold voltage, respectively, and e is the elementary charge. The current density can be represented as $J(x,t) = \sigma E$, where σ and E are the electrical conductivity and the lateral electric field, respectively. Since the carrier density and current density are also mutually related by the continuity equation, a differential equation for $n(x,t)$ can be derived as follows (see Appendix):

$$\frac{\partial n}{\partial t} = \frac{e\mu}{C}\frac{\partial}{\partial x}\left(n\frac{\partial n}{\partial x}\right), \qquad (2)$$

where μ is the carrier mobility. By solving the differential equation numerically under the appropriate initial conditions, the time- and position-dependent carrier density $n(x,t)$ is obtained. As a result of the numerical simulations, the frontal position $x_{\rm front}$ of the channel charges can be approximated as follows (see Appendix):

$$x_{\rm front} \approx 1.623\sqrt{\mu|V_G - V_{\rm TH}|t}. \qquad (3)$$

This equation indicates that the frontal position of the channel charges depends on the square root of the time, as

is observed in the results of the μGM imaging experiments shown in Fig. 4(b). From the square root of the time dependence in Fig. 4(b), we can estimate the carrier mobility to be 1.12 $cm^2\,V^{-1}\,s^{-1}$ by using Eq. (3); this value is consistent with the field-effect mobility from the transfer characteristics under a saturation regime of 1.0 $cm^2\,V^{-1}\,s^{-1}$ (see Fig. S1 [30]).

Figure 4(c) shows comparisons between the experimental and simulated results for the channel charge distribution at various time intervals. We find that the simulated results based on Eqs. (A5) and (A6) closely reproduce the experimental results and we show that the transient carrier conduction through channels of TFTs is well described by the above temporal-response model of the TFTs. Note that the charge distribution at a delay time of 100 ns shows a greater deviation in the area close to the channel-electrode interface, which we will discuss in the next section.

C. Effects of the electrode interface on the transient charge and field distributions

Figure 3(b) shows the expanded line profiles of TR-μGM images around the source electrode, the location of which is indicated by the yellow-colored area. A comparison of the line profiles clearly indicates distinct time evolutions for the positive and negative μGM signals in the channel area close to the channel-electrode interface. The positive μGM signal in the area near the electrode edge exhibits an obvious peak feature at a delay time of 200 ns, whereas the negative μGM signal in the same area remains quite small. We also find that the negative μGM signal exhibits a broad maximum at 200-to-300 ns in the area neighboring the above area.

The peak feature of the positive μGM signal observed at a delay time of 200 ns indicates that a stronger electric field than that in the steady state is applied momentarily after turning on the gate bias. We mention here that the positive μGM signal predominates along the channel-electrode interface, not only in a transient state, but also in a steady state, as seen in Fig. 2. This implies the presence of an electric field around the channel-electrode interfaces. Actually, a clear potential drop has been observed by Kelvin probe force microscopy [35,36]. This is probably caused by the component having a large resistance at the channelelectrode interface. Note that such a transient enhancement of electric fields around electrode interfaces has also been observed by means of the second-harmonic-generation imaging technique [29]. In addition, the time evolution of the negative μGM signal observed at 300 ns indicates that more charges than those in the steady state should accumulate momentarily after the turning on of the gate bias. These features clearly deviate from those expected from the temporal-response model of the TFTs presented above. It is probable that the pentacene layer near the top-contact electrode is damaged by thermal evaporation of the Au electrode in vacuum [37]. In any case, such a temporal evolution near the electrode edge has been shown by the present investigation.

D. Effects of grain boundaries and concentrated carrier traps on transient charge and field distributions

We focus here on the microscopic signal distribution in the localized regions around grain boundaries and within the grains. To observe the transient behavior more clearly, we conduct TR-μGM measurements with a shorter time resolution of 50 ns. Figure 5(a) shows the TR-μGM image and an expanded one at a delay time of 250 ns (additional results for different delay times are shown in Fig. S3 [30]). Although the μGM signal distribution at 250 ns appears to be the same as that in the steady state, a detailed comparison shows that the borders between the positive and negative μGM signals in the transient state (red line) are obviously shifted to the right side of those for the steady state (black line), as shown in Fig. 5(b). To show this shift more clearly, the μGM signal in the transient state is divided by the corresponding signal in the steady state for each pixel, and the results are shown in Fig. 5(c). The shift is clearly seen as a pink-colored region. The first-derivative-like shape seen in the cross-sectional profile in Fig. 5(d) corresponds to the rightward shift of the μGM signal distribution in the transient state. We find that similar features could be seen for all the borders between the

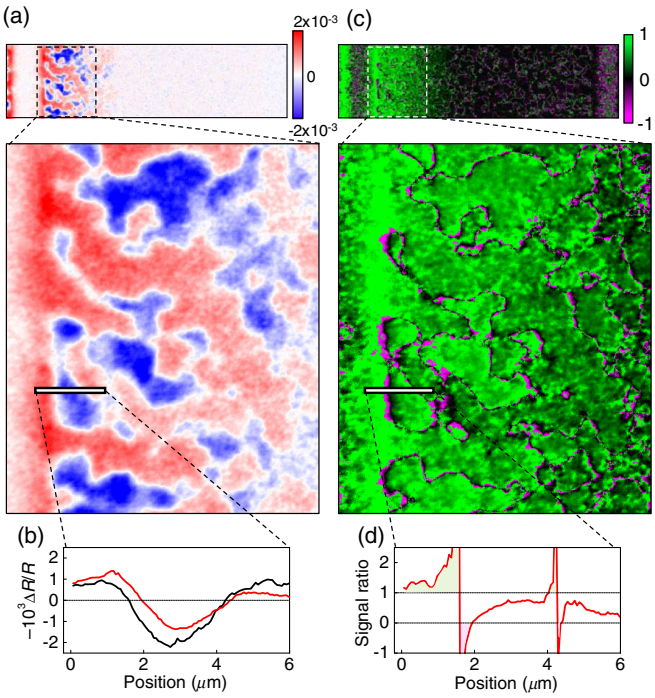

FIG. 5. (a) TR-μGM image and the expanded image at a delay time of 250 ns with a time resolution of 50 ns. (b) Cross-sectional profile on the white line in the TR-μGM image for the transient (red) and steady states (black). (c) TR-μGM image at 250 ns whose intensity is divided by that in a steady state. (d) Cross-sectional profile on the white line the divided image.

positive and negative μGM signals. It is interesting to note that the rightward shift is independent of the signal positional order, i.e., positive-negative or negative-positive. These features can be seen more clearly in Figs. 6(a)–6(c). Crossed-Nicols polarized micrographs are also shown to delineate the geometry of the polycrystalline grains. The border between the positive and negative μGM signals is located at the grain boundary in Fig. 6(a), whereas it is located inside the grains in Figs. 6(b) and 6(c). A rightward shift of the μGM signal distribution is observed in all cases, implying that the distribution of accumulated charges shifts transiently over the whole channel in the direction of carrier transport. Figures 6(d) and 6(e) show additional cases. The positive (or negative) μGM signal is continuous over the grain boundary. In the case of the positive μGM signal shown in Fig. 6(d), the signal intensity in a transient state becomes lower than that in a steady state at the grain boundary. In the case of the negative μGM signal shown in Fig. 6(e), the signal intensity in a transient state increases more than that in a steady state at the grain boundary.

All the cases of transient variations in μGM signal distribution are summarized in Fig. 7. We consider that the variations are caused by either the potential barrier at a grain boundary or by a carrier trap inside a grain. For the case of the negative-positive order of the μGM signal at a grain boundary, an increase in the negative signal is always seen at the front side of the grain boundary. This implies that the carrier transport is limited by the potential barrier of

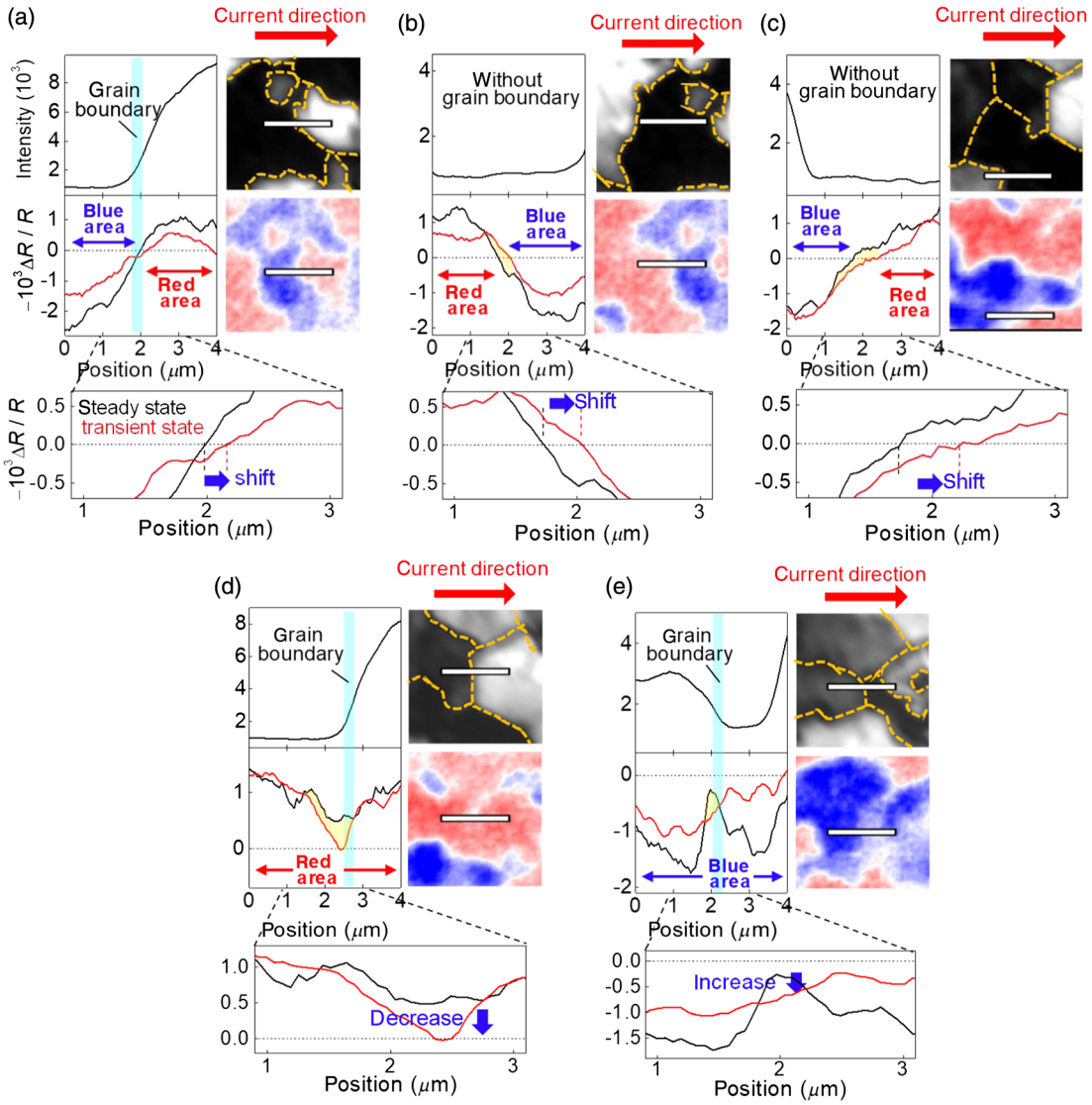

FIG. 6. Cross-sectional profiles on the white lines in crossed-Nicols polarized micrographs and the corresponding TR-μGM images at a delay time of 250 ns obtained with a time resolution of 50 ns. (a) Border between negative and positive μGM signals at a grain boundary. (b) Border between positive and negative μGM signals inside a grain. (c) Border between negative and positive μGM signals inside a grain. (d) Border between positive and positive μGM signals at a grain boundary. (e) Border between negative and negative μGM signals at a grain boundary. Note that the cross-sectional profiles at 250 ns (red) are shown with those in a steady state (black).

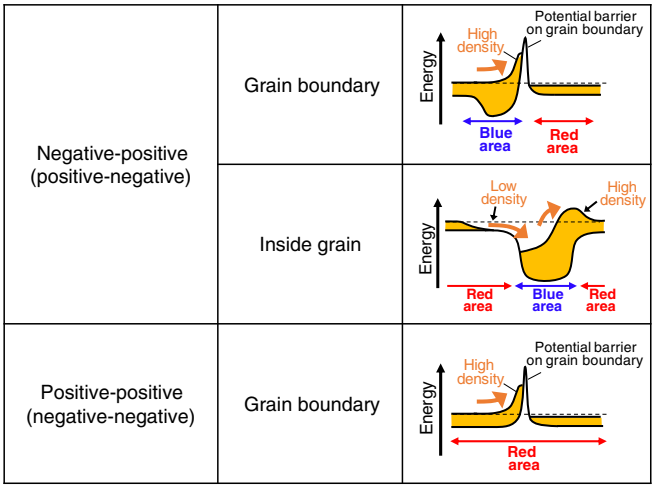

FIG. 7. Schematics showing the microscopic charge distribution in a transient state.

the grain boundary, which causes a transient increase in the carrier density at the front side of the grain boundary. For the case of the positive-positive order of the μGM signal at the grain boundary, a decrease in the positive signal is seen at the front side of the grain boundary. The feature could also be ascribed to a transient increase in the carrier density at the front side of the grain boundary, as the increased carrier density should weaken the leaked gate electric field in this case. Finally, an increase in the negative signal is also observed for the case of the negative-positive order of the μGM signal inside a grain. We consider that the concentrated carrier trap inside the grains affects the polarity in the μGM signals, and that the carrier transport across the concentrated carrier trap should be limited by the trap depth, which causes a transient increase in the carrier density in the region to escape from a concentration of carrier traps.

IV. CONCLUSIONS

We investigate the temporal evolution of the channel current and accumulated charges in polycrystalline pentacene TFTs by means of a nanosecond TR-μGM imaging technique. A series of TR-μGM images clearly shows the gradual propagation of μGM signals within the polycrystalline channel layers. In all the TR-μGM images, the positive and negative μGM signals are observed to be distributed inhomogeneously with roughly (but not exactly) identical spatial distribution in the steady-state image, demonstrating that these positive and negative μGM signals correspond to channel charges and leaked gate fields, respectively. We find that the gradual expansion of the positive and negative μGM signals is simultaneous, with identical frontal positions. This affords clear evidence that the local electric fields within the gate dielectric layers become effective when the hole carriers are charged up within the channels. Based on these observations, the temporal evolution of the channel current and accumulated charges are modeled by applying a temporal-response model of organic TFTs, which fundamentally reproduces the observed TR-μGM images and is highly consistent with the transport characteristics. A slight deviation from the model is found in the initial TR-μGM images at around the channel-electrode interface, indicating that the electric field effect is initially concentrated due to the high contact resistance or carrier injection barrier. The effect of grain boundaries is also visualized by the TR-μGM images, showing that potential barriers at the grain boundaries or concentrations of carrier traps cause the temporal variations in the μGM signals. These results show that the μGM imaging technique is informative in revealing how charge carriers prevail and propagate microscopically over channel layers, thereby clarifying the limiting factors in the polycrystalline channel layers in organic TFTs.

ACKNOWLEDGMENTS

This work is supported by the Japan Society for The Promotion of Science (JSPS) KAKENHI (Grants No. JP16H05976, No. JP17H05144, and No. JP26246014), and by the Japan Science and Technology Agency (JST) through the Strategic Promotion of Innovative Research and Development Program (S-Innovation).

APPENDIX: TEMPORAL-RESPONSE MODEL OF THE TFTS

The transient charge-carrier transport in the channels of TFTs is modeled by using the three variables $n(x,t)$, $J(x,t)$, and $V(x,t)$. The variable $n(x,t)$ is directly associated with $V(x,t)$ by the capacitance of the gate dielectric layer, as shown in Eq. (1). The variable $J(x,t)$ is represented as follows:

$$J(x,t) = \sigma E = -e\mu n(x,t)\frac{\partial V(x,t)}{\partial x}. \tag{A1}$$

The variables $n(x,t)$ and $J(x,t)$ are related by the continuity equation as follows:

$$\frac{\partial n(x,t)}{\partial t} = -\frac{1}{e}\frac{\partial J(x,t)}{\partial x}. \tag{A2}$$

From Eqs. (1), (A1), and (A2), a differential equation for $n(x,t)$ is finally derived as Eq. (2). Under the initial condition of $n(x,0) = 0$ and the boundary conditions of $n(0,t) = C|V_G - V_{\rm th}|/e$ and $n(\infty,t) = 0$, Eq. (2) can be rewritten as follows:

$$\frac{\partial u}{\partial t} = \alpha\frac{\partial}{\partial x}\left(u\frac{\partial u}{\partial x}\right), \tag{A3}$$

where $\alpha \equiv \mu|V_G - V_{\rm th}|$. The dimensionless parameter $u(x,t)$ of the carrier density is defined as

$$u(x,t) \equiv \frac{en(x,t)}{C|V_G - V_{\rm th}|}. \tag{A4}$$

By using Eq. (A4), the initial condition and the boundary conditions can be rewritten as $u(x,0) = 0$, $u(0,t) = 1$, and $u(\infty,t) = 0$. The variables x and t in Eq. (A3) can be unified by using the Boltzmann transform of $s \equiv x/\sqrt{\alpha t}$ [38] as follows:

$$-\frac{s}{2}f' = (f')^2 + ff'', \tag{A5}$$

where

$$u(x,t) = f\left(\frac{x}{\sqrt{\alpha t}}\right) = f(s). \tag{A6}$$

We solve Eq. (A5) numerically, and our results are shown in Fig. S5 [30]. The obtained frontal position of the $f(s)$ is ~1.623, which finally gives Eq. (3).

[1] W. G. Hawkins, Polycrystalline-silicon device technology for large-area electronics, IEEE Trans. Electron Devices **33**, 477 (1986).

[2] K. Takei, T. Takahashi, J. C. Ho, H. Ko, A. G. Gillies, P. W. Leu, R. S. Fearing, and A. Javey, Nanowire active-matrix circuitry for low-voltage macroscale artificial skin, Nat. Mater. **9**, 821 (2010).

[3] A. C. Arias, J. D. MacKenzie, I. McCulloch, J. Rivnay, and A. Salleo, Materials and applications for large area electronics: Solution-based approaches, Chem. Rev. **110**, 3 (2010).

[4] S. D. Brotherton, Polycrystalline silicon thin film transistors, Semicond. Sci. Technol. **10**, 721 (1995).

[5] T. Serikawa and F. Omata, High-quality polycrystalline Si TFTs fabricated on stainless-steel foils by using sputtered Si films, IEEE Trans. Electron Devices **49**, 820 (2002).

[6] C.-Y. Chen, J.-W. Lee, S.-D. Wang, M.-S. Shieh, P.-H. Lee, W.-C. Chen, H.-Y. Lin, K.-L. Yeh, and T.-F. Lei, Negative bias temperature instability in low-temperature polycrystalline silicon thin-film transistors, IEEE Trans. Electron Devices **53**, 2993 (2006).

[7] T. Kamiya, K. Nomura, and H. Hosono, Present status of amorphous In-Ga-Zn-O thin film transistors, Sci. Technol. Adv. Mater. **11**, 044305 (2010).

[8] L. Petti, N. Münzenrieder, C. Vogt, H. Faber, L. Büthe, G. Cantarella, F. Bottacchi, T. D. Anthopoulos, and G. Tröster, Metal oxide semiconductor thin-film transistors for flexible electronics, Appl. Phys. Rev. **3**, 021303 (2016).

[9] M. Engel, J. P. Small, M. Steiner, M. Freitag, A. A. Green, M. C. Hersam, and P. Avouris, Thin film nanotube transistors based on self-assembled, aligned, semiconducting carbon nanotube arrays, ACS Nano **2**, 2445 (2008).

[10] D.-M. Sun, M. Y. Timmermans, Y. Tian, A. G. Nasibulin, E. I. Kauppinen, S. Kishimoto, T. Mizutani, and Y. Ohno, Flexible high-performance carbon nanotube integrated circuits, Nat. Nanotechnol. **6**, 156 (2011).

[11] C. R. Kagan, D. B. Mitzi, and C. D. Dimitrakopoulos, Organic-inorganic hybrid materials as semiconducting channels in thin-film field-effect transistors, Science **286**, 945 (1999).

[12] T. M. Brenner, D. A. Egger, L. Kronik, G. Hodes, and D. Cahen, Hybrid organic-inorganic perovskites: Low-cost semiconductors with intriguing charge-transport properties, Nat. Rev. Mater. **1**, 15007 (2016).

[13] Y. Zhao and K. Zhu, Organic-inorganic hybrid lead halide perovskites for optoelectronic and electronic applications, Chem. Soc. Rev. **45**, 655 (2016).

[14] T. Someya, T. Sekitani, S. Iba, Y. Kato, H. Kawaguchi, and T. Sakurai, A large-area, flexible pressure sensor matrix with organic field-effect transistors for artificial skin applications, Proc. Natl. Acad. Sci. U.S.A. **101**, 9966 (2004).

[15] J. Rivnay, L. H. Jimison, J. E. Northrup, M. F. Toney, R. Noriega, S. Lu, T. J. Marks, A. Facchetti, and A. Salleo, Large modulation of carrier transport by grain-boundary molecular packing and microstructure in organic thin films, Nat. Mater. **8**, 952 (2009).

[16] A. Facchetti, π-conjugated polymers for organic electronics photovoltaic cell applications, Chem. Mater. **23**, 733 (2011).

[17] P. M. Voyles, J. E. Gerbi, M. M. J. Treacy, J. M. Gibson, and J. R. Abelson, Absence of an Abrupt Phase Change from Polycrystalline to Amorphous in Silicon with Deposition Temperature, Phys. Rev. Lett. **86**, 5514 (2001).

[18] G. Horowitz, M. E. Hajlaoui, and R. Hajlaoui, Temperature and gate voltage dependence of hole mobility in polycrystalline oligothiophene thin film transistors, J. Appl. Phys. **87**, 4456 (2000).

[19] C. D. Dimitrakopoulos and P. R. L. Malenfant, Organic thin film transistors for large area electronics, Adv. Mater. **14**, 99 (2002).

[20] V. Coropceanu, J. Cornil, D. A. da Silva Filho, Y. Olivier, R. Silbey, and J.-L. Brédas, Charge transport in organic semiconductors, Chem. Rev. **107**, 926 (2007).

[21] S. Matsuoka, J. Tsutsumi, T. Kamata, and T. Hasegawa (to be published).

[22] T. Manaka, S. Kawashima, and M. Iwamoto, Charge modulated reflectance topography for probing in-plane carrier distribution in pentacene field-effect transistors, Appl. Phys. Lett. **97**, 113302 (2010).

[23] C. Sciascia, N. Martino, T. Schuettfort, B. Watts, G. Grancini, M. R. Antognazza, M. Zavilani-Rossi, C. R. McNeill, and M. Caironi, Sub-micrometer charge modulation microscopy of a high mobility polymeric n-channel field-effect transistor, Adv. Mater. **23**, 5086 (2011).

[24] A. R. Davis, L. N. Pye, N. Katz, J. A. Hudgings, and K. R. Carter, Spatially mapping charge carrier density and defects in organic electronics using modulation-amplified reflectance spectroscopy, Adv. Mater. **26**, 4539 (2014).

[25] J. Tsutsumi, S. Matsuoka, T. Yamada, and T. Hasegawa, Gate-modulation of organic thin-film transistor arrays: Visualization of distributed mobility and dead pixels, Org. Electron. **25**, 289 (2015).

[26] R. Steyrleuthner, M. Schubert, F. Jaiser, J. C. Blakesley, Z. Chen, A. Faccetti, and D. Neher, Bulk electron transport and charge injection in a high mobility n-type semiconducting polymer, Adv. Mater. **22**, 2799 (2010).

[27] C. Liewald, D. Reiser, C. Westermeier, and B. Nickel, Photocurrent microscopy of contact resistance and charge carrier traps in organic field-effect transistors, Appl. Phys. Lett. **109**, 053301 (2016).

[28] T. Manaka, E. Lim, R. Tamura, and M. Iwamoto, Direct imaging of carrier motion in organic transistors by optical second-harmonic generation, Nat. Photonics **1**, 581 (2007).

[29] T. Manaka, F. Liu, M. Weis, and M. Iwamoto, Studying transient carrier behaviors in pentacene field effect transistors using visualized electric field migration, J. Phys. Chem. C **113**, 10279 (2009).

[30] See Supplemental Material at http://link.aps.org/supplemental/10.1103/PhysRevApplied.9.024025 for additional experimental and numerical calculation results.

[31] S. Haas, H. Matsui, and T. Hasegawa, Field-modulation spectroscopy of pentacene thin films using field-effect devices: Reconsideration of the excitonic structure, Phys. Rev. B **82**, 161301(R) (2010).

[32] L. Sebastian, G. Weiser, and H. Bässler, Charge transfer transitions in solid tetracene and pentacene studied by electroabsorption, Chem. Phys. **61**, 125 (1981).

[33] J. Tsutsumi, S. Matsuoka, I. Osaka, R. Kumai, and T. Hasegawa, Reduced exchange narrowing caused by gate-induced charge carriers in high-mobility donor-acceptor copolymers, Phys. Rev. B **95**, 115306 (2017).

[34] W. Shockley, Transistor electronics: Imperfections, unipolar and analog transistors, Proc. IRE **40**, 1289 (1952).

[35] L. Bürgi, H. Sirringhaus, and R. H. Friend, Noncontact potentiometry of polymer field-effect transistors, Appl. Phys. Lett. **80**, 2913 (2002).

[36] K. P. Puntambekar, P. V. Pesavento, and C. D. Frisbie, Surface potential profiling and contact resistance measurements on operating pentacene thin-film transistors by Kelvin probe force microscopy, Appl. Phys. Lett. **83**, 5539 (2003).

[37] P. V. Pesavento, R. J. Chesterfield, C. R. Newman, and C. D. Frisbie, Gated four-probe measurements on pentacene thin-film transistors: Contact resistance as a function of gate voltage and temperature, J. Appl. Phys. **96**, 7312 (2004).

[38] L. Boltzmann, About the integration of the diffusion equation in the case of variable diffusion coefficients, Ann. Phys. **289**, 959 (1894).